J. Fluid Mech. (2017), *vol.* 817, *pp.* 388–405. © Cambridge University Press 2017
doi:10.1017/jfm.2017.66

Dynamics of a macroscopic elastic fibre in a polymeric cellular flow

Qiang Yang[1] **and Lisa Fauci**[1,†]

[1]Department of Mathematics, Tulane University, New Orleans, LA 70118, USA

(Received 7 July 2016; revised 24 January 2017; accepted 25 January 2017;
first published online 20 March 2017)

We study the dynamics and transport of an elastic fibre in a polymeric cellular flow. The macroscopic fibre is much larger than the infinitesimal immersed polymer coils distributed in the surrounding viscoelastic fluid. Here we consider low-Reynolds-number flow using the Navier–Stokes/Fene-P equations in a two-dimensional, doubly periodic domain. The macroscopic fibre supports both tensile and bending forces, and is fully coupled to the viscoelastic fluid using an immersed boundary framework. We examine the effects of fibre flexibility and polymeric relaxation times on fibre buckling and transport as well as the evolution of polymer stress. Non-dimensional control parameters include the Reynolds number, the Weissenberg number, and the elasto-viscous number of the macroscopic fibre. We find that large polymer stresses occur in the fluid near the ends of the fibre when it is compressed. In addition, we find that viscoelasticity hinders a fibre's ability to traverse multiple cells in the domain.

Key words: flow–structure interactions, non-Newtonian flows, viscoelasticity

1. Introduction

The motion of flexible fibres suspended in a fluid is fundamental to many biological and physical processes. These fibres could be actively generating propulsive forces or passively transported by the flow. Respiratory cilia may be thought of as actuated elastica that are responsible for mucus clearance, while sperm flagella are actuated elastica responsible for mammalian fertilization (Fauci & Dillon 2006). Flexible diatom chains passively move in the turbulent ocean and account for much of the Earth's primary production (Karp-Boss & Jumars 1998). Actin filaments and DNA strands are also examples of passive elastic fibres that may bend in a moving fluid (Kantsler & Goldstein 2012; Harasim *et al.* 2013). In industry, sorting pulp fibres based on their flexibility is central to the paper-making process (Stockie & Green 1998).

Early experiments by Forgacs & Mason (1959) catalogued the shape deformations of elastomer fibres in shear, and noted that, for a given fluid viscosity and shear rate, there was a critical length above which the fibres buckled. More recently, the orbits and buckling of flexible fibres in a Newtonian shear flow have been analysed using slender-body hydrodynamics (Becker & Shelley 2001; Tornberg & Shelley 2007),

† Email address for correspondence: fauci@tulane.edu

bead models (Skjetne, Ross & Klingenberg 1997) and computational models that fully couple fibre forces with fluid dynamics (Stockie & Green 1998; Nguyen & Fauci 2014). More complicated transport of fibres occurs in cellular flows that are formed by counter-rotating vortices. In the absence of fibres, streamlines within the cellular regions are closed. Here, hyperbolic stagnation points are connected by stable and unstable manifolds (Young & Shelley 2007; Wandersman *et al.* 2010; Quennouz *et al.* 2015). Young & Shelley (2007) characterized the stretch–coil instability of fibres in such cellular flows of a viscous Stokesian fluid. They simulated an elastic fibre immersed in a four-roll mill and showed that buckling instabilities modulated transport of fibres through the cellular domain. In particular, they characterized the fibres as 'random walkers' that choose an escape direction away from the stagnation point based upon their internal bending properties and their shape as they near the compressive region. The buckling threshold was determined by the elasto-viscous number of the fibre, which is the ratio of the fluid's viscous forces to the fibre's elastic force. Recent laboratory experiments by Wandersman *et al.* (2010) confirmed this buckling threshold. These experiments showed that the fibre's ability to escape the cellular regions increased with their flexibility. Most recently, through coordinated experimental and theoretical studies, Quennouz *et al.* (2015) found that the fibre buckling probability depends not only on the elasto-viscous number, but also on the entry position and orientation. The entrapment of fibres in the cellular regions is also highly dependent on the entry position and entry orientation. Recently, Manikantan & Saintillan (2013) analysed the effect of thermal fluctuations on the transport of fibres in cellular flows, and showed that such fluctuations enhance the trapping within vortical cells.

As in the case of a cilium beating in mucus, in many biological applications a macroscopic fibre may be interacting with a fluid that has an embedded microstructure. Here we study the motion of a flexible macroscopic fibre in a cellular flow where the surrounding fluid is viscoelastic. We choose the Fene-P modification of an Oldroyd-B description, which models the viscoelastic fluid as a Newtonian solvent with polymers embedded (Larson 1998; Phan-Thien 2002). Numerical studies of such Stokesian viscoelastic cellular flows without a macroscopic fibre have been performed by Thomases & Shelley (2007). While the geometry of the flow is driven by a time-independent background force, polymer stresses coupled to the fluid equations result in flows that are not constant in time. They observed the emergence of singular structures in the polymer stress field in Oldroyd-B fluids for large enough Weissenberg number – the ratio of polymer relaxation time to the flow time scale. However, when finite chain lengths were enforced using a Fene-P modification, the maximum values of stress were reduced.

Here we examine the transport of an immersed elastic macroscopic fibre in a two-dimensional, doubly periodic cellular flow. A Navier–Stokes fluid with additional polymer stresses due to Fene-P description is driven by a background force. We present the mathematical formulation of the coupled fluid–polymer fibre system, and discuss the non-dimensional control parameters that govern the dynamics. We examine the effects of Weissenberg number and elasto-viscous number on fibre dynamics, transport and their ability to escape cellular regions.

2. Mathematical model

We consider an elastic flexible fibre immersed in a four-roll mill background flow (Young & Shelley 2007; Wandersman *et al.* 2010). In the absence of a fibre or

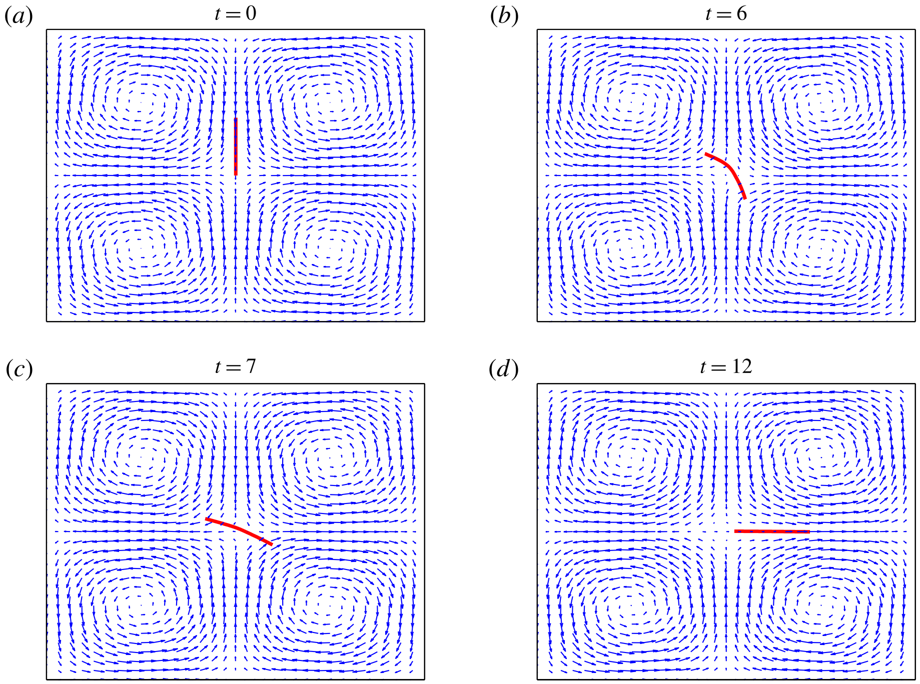

FIGURE 1. (Colour online) Fibre configurations at different times at $Re = 2.5$, $Wi = 1$ and $\eta = 370$. This fairly stiff fibre approaches the stagnation point at the centre, bends, regains its straight configuration and then moves away from the stagnation point along the outgoing streamline to the right.

viscoelasticity, the velocity field of this cellular, doubly periodic flow on the domain $\tilde{\Omega} = [-W, W] \times [-W, W]$ is

$$\boldsymbol{u}_b = u_0 \begin{pmatrix} \sin\left(\dfrac{\pi}{W}x\right) \cos\left(\dfrac{\pi}{W}y\right) \\ -\cos\left(\dfrac{\pi}{W}x\right) \sin\left(\dfrac{\pi}{W}y\right) \end{pmatrix}. \tag{2.1}$$

This background velocity may be generated by adding a time-independent external force density to the Navier–Stokes equations. Figure 1(*a*) shows this vortical background flow, where vertical compression and horizontal stretching occur near the central stagnation point. Within this domain, we will introduce a fibre of length L. We choose the physical parameters as shown in table 1. These parameters largely follow the experiments of Wandersman *et al.* (2010), except that here we choose a cellular length of $W = \pi$ cm while their experiments were performed with $W = 3$ cm.

We choose our dimensional length scale to be the vortical cell diameter W, and the time scale to be the inverse of the maximal extension rate $\dot{\gamma} = \pi u_0/W$. We assume that the viscoelastic fluid dynamics is described by the coupled non-dimensional Navier–

Quantity	Description	Value	Units
ρ	Fluid density	1.25	g cm^{-3}
μ	Solvent viscosity	0.4	g cm^{-1} s^{-1}
u_0	Maximal velocity	0.08	cm s^{-1}
W	Cellular length	π	cm
L	Fibre length	0.4π	cm
r	Effective fibre radius	0.025	cm
ϵ	Aspect ratio r/L	$0.0625/\pi$	—
Re	Reynolds number	2.5	
Wi	Weissenberg number	0.0–5.0	
η	Elasto-viscous number	370–2960	

TABLE 1. Physical parameters.

Stokes/Fene-P equations in the domain $\varOmega=[-1, 1]\times[-1, 1]$ with periodic boundary conditions:

$$Re\left(\frac{\partial \boldsymbol{u}}{\partial t}+\boldsymbol{u}\boldsymbol{\cdot}\nabla\boldsymbol{u}\right)=-\nabla p+\Delta\boldsymbol{u}+\beta\,\nabla\boldsymbol{\cdot}\boldsymbol{S}+\boldsymbol{f}+\boldsymbol{g}, \tag{2.2}$$

$$\nabla\boldsymbol{\cdot}\boldsymbol{u}=0, \tag{2.3}$$

$$\frac{\partial\boldsymbol{C}}{\partial t}+\boldsymbol{u}\boldsymbol{\cdot}\nabla\boldsymbol{C}-(\nabla\boldsymbol{u}\boldsymbol{C}+\boldsymbol{C}\nabla\boldsymbol{u}^{\mathrm{T}})=-Wi^{-1}(\boldsymbol{S}-\boldsymbol{I}), \tag{2.4}$$

$$\boldsymbol{S}=\frac{\boldsymbol{C}}{1-\mathrm{tr}(\boldsymbol{C})/\mathcal{L}^2}. \tag{2.5}$$

The non-dimensional velocity and pressure are $\boldsymbol{u}=(u, v)$ and p, respectively, and the Reynolds number is $Re=\rho\pi W u_0/\mu$. The Weissenberg number, $Wi=\tau_p/\tau_f$, is the ratio of the polymer relaxation time τ_p and the time scale of the flow $\tau_f=(\dot{\gamma})^{-1}$. The dimensionless stress tensor $\boldsymbol{C}$ has been scaled by G, the isotropic stress arising from thermodynamic fluctuations of the polymer chains in the absence of flow. Note that $G=\kappa TV$, where κ is the Boltzmann constant, T is temperature and V is the number of polymer chains per unit volume (Larson 1998). The Fene-P stress tensor $\boldsymbol{S}$ penalizes the extensibility of the infinitesimal polymer chains, and $\mathcal{L}$ represents the ratio of the maximal polymer length when stretched to the polymer length when coiled. Here $\boldsymbol{S}$ represents the extra stress generated by the transport and distension of the polymer field, and is coupled to the Navier–Stokes equation with the parameter $\beta=G\tau_f/\mu$. Note that $\beta\cdot Wi$ is a physical quantity that measures the ratio of polymer viscosity to solvent viscosity. As in Thomases & Shelley (2007), here we choose $\mathcal{L}^2=50$ and $\beta Wi=0.5$.

In the momentum equation (2.2), $\boldsymbol{g}(\boldsymbol{x})$ is the external force density chosen to achieve the background velocity field,

$$\boldsymbol{g}=\frac{Re}{\pi}\begin{pmatrix}\cos(\pi x)\sin(\pi x)\\ \cos(\pi y)\sin(\pi y)\end{pmatrix}+2\pi\begin{pmatrix}\sin(\pi x)\cos(\pi y)\\ -\cos(\pi x)\sin(\pi y)\end{pmatrix}, \tag{2.6}$$

and $\boldsymbol{f}$ is the force density imparted to the fluid by the fibre,

$$\boldsymbol{f}(\boldsymbol{x},t)=\int_D \boldsymbol{F}(s, t)\delta(\boldsymbol{x}-\boldsymbol{X}(s, t))\,\mathrm{d}s. \tag{2.7}$$

Here the position of the fibre D is given by $\boldsymbol{X}(s,t)$, with s a material coordinate and δ the two-dimensional Dirac delta function. The fibre is taken to be a generalized Euler elastica whose equilibrium configuration is straight. The fibre supports forces $\boldsymbol{F}=-(\partial E/\partial \boldsymbol{X})$ that are derived from tensile (E_t) and bending (E_b) energies,

$$E=E_t+E_b=\frac{1}{2}\sigma_s\int_D\left(\left\|\frac{\partial \boldsymbol{X}}{\partial s}\right\|-1\right)^2\mathrm{d}s+\frac{1}{2}\sigma_b\int_D\left\|\frac{\partial^2 \boldsymbol{X}}{\partial s^2}\right\|^2\mathrm{d}s, \tag{2.8}$$

where σ_s is a non-dimensional tensile stiffness and σ_b is a non-dimensional bending stiffness. In the simulations presented below, we choose σ_s large enough so that the fibre remains nearly inextensible, with deviations from its equilibrium arclength of no more than 3 %. The non-dimensional bending stiffness σ_b may be varied to change fibre flexibility, and is related to the dimensional bending rigidity EI of the fibre by

$$\sigma_b=\frac{EI}{4\pi^2\mu u_0 W^2 r}. \tag{2.9}$$

The relative importance of flow forces to elastic forces is measured by

$$\eta=\frac{8\pi\mu\dot{\gamma}L^4}{cEI}, \tag{2.10}$$

where $c=-\log(\epsilon^2 e)$. As in Quennouz *et al.* (2015), we refer to η as the elasto-viscous number. This non-dimensional control parameter has also been referred to as 'effective viscosity' in Tornberg & Shelley (2007), 'effective flow forcing' in Nguyen & Fauci (2014) and 'sperm number' in Wandersman *et al.* (2010). In the simulations presented below, we choose the bending stiffness σ_b so that the range of the elasto-viscous number η is as stated in table 1.

The system is closed by enforcing the no-slip condition that requires the material points of the immersed fibre to move at the fluid velocity defined at those points:

$$\frac{\partial \boldsymbol{X}}{\partial t}=\boldsymbol{u}(\boldsymbol{X}(s,t),t)=\int_\Omega \boldsymbol{u}(\boldsymbol{x},t)\delta(\boldsymbol{x}-\boldsymbol{X}(s,t))\,\mathrm{d}\boldsymbol{x}. \tag{2.11}$$

The formulation of the coupled fluid–fibre–viscoelastic system described above is readily discretized using an immersed boundary formulation, as in Teran, Fauci & Shelley (2010), Chrispell, Fauci & Shelley (2013) and Thomases & Guy (2014). The fluid velocity, pressure and polymer stress tensors are defined on an $M\times M$ finite difference grid, and the centreline of the macroscopic fibre is discretized using N points. The tensile and bending forces supported on the Lagrangian fibre are spread to the grid using discretized Dirac delta functions (Peskin 2002). Within this immersed boundary framework, we associate an effective radius of the fibre to be one grid spacing, which accounts for most of the support of the forces along the one-dimensional fibre centreline. A time-splitting method is used to evolve the momentum equation and the polymer stress equation. The momentum equation is updated using the formally second-order method of Lai & Peskin (2000), and the polymer stress equation is updated using the square-root method of Balci *et al.* (2011). Both velocity and polymer stress are evolved using a second-order Runge–Kutta method. In the simulations presented below, we discretize the fluid domain using a lattice of 256×256 grid points and the fibre, whose length is not varied, is discretized as a one-dimensional curve with $N=103$ points. Because of the properties of the discretized Dirac delta function, which the spreads the fibre forces to nearby grid points, the effective radius of the fibre is taken to be a single grid spacing. This interpretation is used to identify the elasto-viscous number of the coupled system.

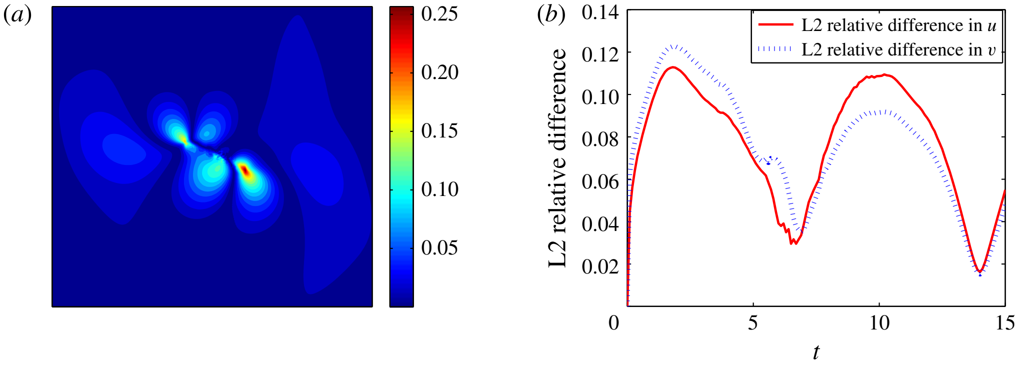

FIGURE 2. (Colour online) (*a*) Contour plot of the difference in vertical velocity components at $t=7$ between the coupled fibre–viscoelastic system shown in figure 1(*c*) and a simulation with no immersed fibre, normalized by the vertical velocity of the fibre-free case. (*b*) The relative L2 norm of the difference between the velocities (both horizontal and vertical components) of the coupled fibre–viscoelastic system and the fibre-free case for time $0\leqslant t\leqslant 15$.

3. A case study

Here we examine the motion of an elastic macroscopic fibre immersed in a polymeric fluid that is driven by external forcing. The Reynolds number $Re = 2.5$ is small, but non-zero, the elasto-viscous number is $\eta = 370$ and the Weissenberg number $Wi = 1$. We interpret the effective radius of the one-dimensional fibre to be the grid spacing, giving an aspect ratio $\epsilon = r/L \approx 0.02$. This aspect ratio is at the high end of those reported in Quennouz *et al.* (2015) and approximately three times the aspect ratio of the fibres used in the experiments of Wandersman *et al.* (2010). At time $t=0$ the fibre is placed vertically in the domain, offset slightly from the midline (along $x = 1.2\times 10^{-3}$ with its lowest point at $y = 1.2\times 10^{-6}$). Initially, the fibre is in its equilibrium, straight and unstretched configuration (figure 1*a*). The velocity field was initialized to be the cellular vortical flow given by (2.1), and the polymer stress tensor $\boldsymbol{S}$ was initialized to be the identity. As the fibre nears the stagnation point along the stable manifold, it buckles slightly (figure 1*b*). At time $t=7$ we see that the fibre is nearly straight again and follows a path away from the stagnation point along the horizontal unstable manifold (figure 1*c*,*d*). In related computational studies that examined motion of an inextensible fibre in a Newtonian–Stokes cellular flow, Young & Shelley (2007) found that the onset of a buckling instability occurred for elasto-viscous number $\eta \approx 328$, and later experimental studies by Wandersman *et al.* (2010) found this threshold value to be $\eta \approx 400$. The elasto-viscous number of the fairly rigid fibre in figure 1 is near these buckling thresholds, and, while demonstrating some bending, does not exhibit dramatic shape changes.

While the Reynolds number chosen here $Re=2.5$ is in the range of the experiments in Wandersman *et al.* (2010), the experiments of Quennouz *et al.* (2015) were performed at lower values. We did run simulations as in figure 1 at the lower Reynolds numbers $Re=0.5$ and 1.0 and found little difference in the fibre dynamics.

The presence of the fibre influences the local flow structure. In order to measure this influence, we ran a simulation using the same parameters as in the present case study, but without the immersed fibre. Figure 2(*a*) shows a contour plot of the difference in vertical velocity components at $t=7$ between the coupled fibre–viscoelastic system

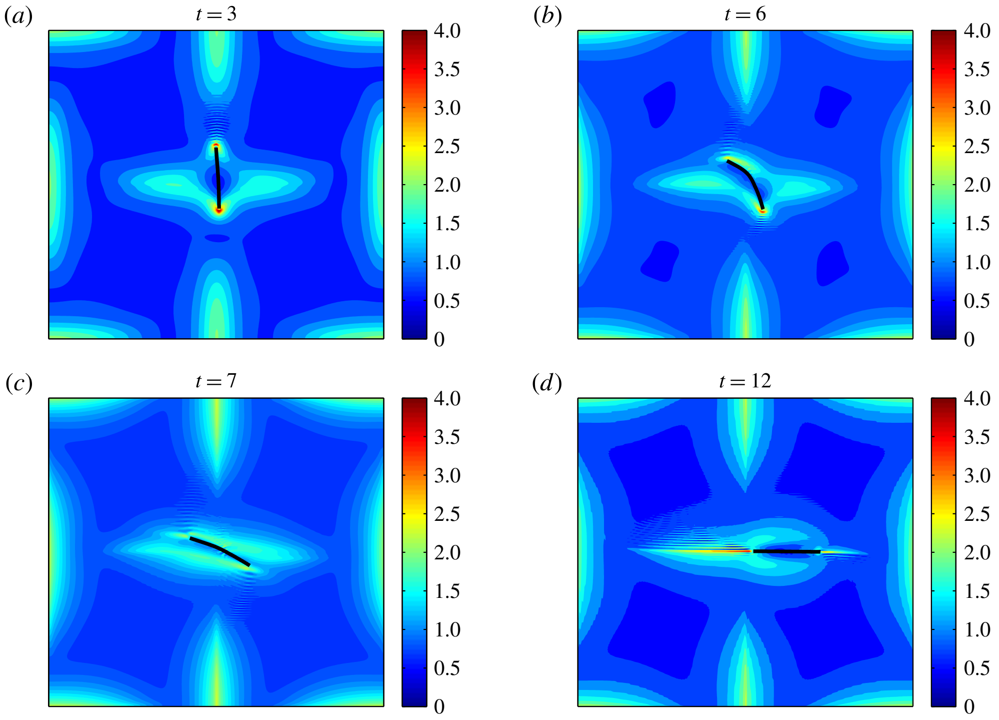

FIGURE 3. (Colour online) Snapshots of contours of the $\log(\mathrm{tr}\,\boldsymbol{S})$ and the macroscopic fibre. Note that $\mathrm{tr}\,\boldsymbol{S}$ measures the mean squared distension of polymer coils. Here $Re = 2.5$, $Wi = 1$ and $\eta = 370$.

shown in figure 1(*c*) and the simulation with no immersed fibre, normalized by the vertical velocity of the fibre-free case. We see that the differences are localized near the fibre, and the vertical velocities near the fibre endpoints are altered nearly 25 %. Figure 2(*b*) shows the L2 norm of the difference between the two components of velocity, normalized by the L2 norm of velocity in the fibre-free case as a function of time. Interestingly, the fibre has the least effect on the velocity field at times that correspond to buckling events (near time $t = 6$, for instance).

Figure 3 shows contour plots of the log of the trace of the stress field $\boldsymbol{S}$. Note that $\mathrm{tr}(\boldsymbol{S})$ measures the mean squared distension of polymer coils. As demonstrated by Thomases & Shelley (2007) for cellular viscoelastic flows without an immersed macroscopic fibre, stress concentrates on a region emanating from the stagnation point in the extensional direction. For the small Weissenberg number $Wi = 1$, the polymers are slowly stretched and this stretch is limited by the Fene-P penalization. In fact, in all of the simulations presented here, the Weissenberg numbers are small enough and the runtime is small enough that the threshold of instability of the cellular flow is not reached. Figure 3(*a*) shows that when the fibre is almost straight and is being compressed, large polymer stresses are concentrated near its ends. At this instance, the fibre's tensile energy is large as it tries to maintain its length (figure 7*a*). The contours in figure 3(*b*) show that as the fibre starts to bend the polymer stresses decrease near its ends, and when it straightens in figure 3(*c*) the polymer stress is distributed along the fibre. As the fibre moves along the unstable horizontal direction, we again see large polymer stretching near its ends.

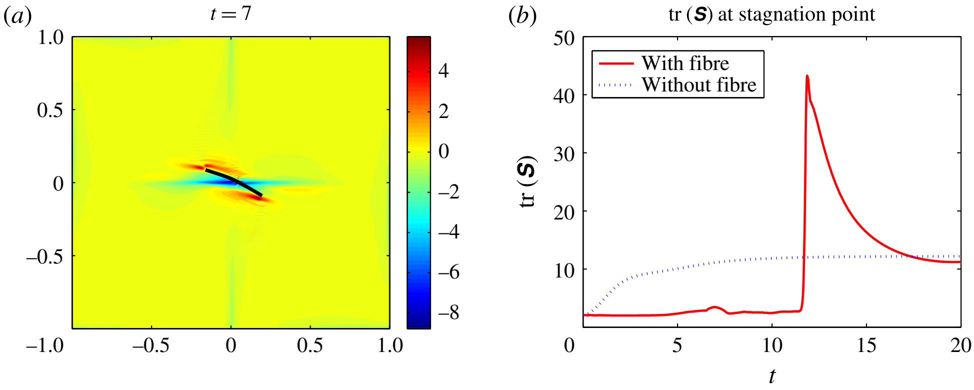

FIGURE 4. (Colour online) (*a*) At time $t=7$, contours of the difference between tr($\boldsymbol{S}$) in the fibre–viscoelastic system and that in the corresponding fibre-free viscoelastic system. (*b*) Values of tr($\boldsymbol{S}$) at the stagnation point in both the fibre–viscoelastic system and the fibre-free viscoelastic system as a function of time. Here $Re=2.5$, $Wi=1$ and $\eta=370$.

In order to determine how the presence of the macroscopic fibre affects the polymer stress field, we examine the difference between tr($\boldsymbol{S}$) with a fibre and tr($\boldsymbol{S}$) in a simulation with no fibre. Figure 4(*a*) shows contours of this difference at time $t = 7$. We see positive values around the ends of the fibre, which demonstrate that there is extra distension of the polymers caused by the fibre locally at its ends. However, along the extensional horizontal direction around the stagnation point, negative contours indicate that the presence of the fibre limits the polymer distension there. Figure 4(*b*) plots the evolution of tr($\boldsymbol{S}$) evaluated at the stagnation point for both the coupled fibre–viscoelastic system and the fibre-free system. The dotted blue line, indicating tr($\boldsymbol{S}$) in the absence of a fibre, shows that this value stabilizes to a constant, as the Fene-P penalization limits the polymer stretching. The solid red curve indicates tr($\boldsymbol{S}$) at the stagnation point for the fibre–viscoelastic system. Note that up until approximately $t = 12$, distension of the polymers at the stagnation point falls considerably below that in the fibre-free system. As the fibre moves away from the stagnation point, it carries along stretched polymers at its end to the fixed location of the stagnation point, and tr($\boldsymbol{S}$) spikes. As the fibre exits the cell, the distension of polymers at the stagnation point relaxes to the value in the fibre-free case.

We may also visualize the symmetric, positive definite stress field $\boldsymbol{S}$ using ellipses whose axes align with eigenvectors of $\boldsymbol{S}$ and whose lengths are the two positive real eigenvalues. The major axis tells us how much and in what direction the polymers are stretched locally. Initially the stress fields are isotropic, and the added polymer stress ellipses are unit circles. Figure 5(*a*) shows the fibre at $t=12$ and the corresponding stress ellipses. Figure 5(*b*) shows the horizontal component of the fluid velocity along the x-axis of the domain at the corresponding time $t=12$. We see that this velocity is approximately constant in the interval of the axis that is occupied by the fibre at that time, indicating that it is moving uniformly to the right.

When this coupled fibre–viscoelastic system is run until time $t = 80$, the fibre meanders through the periodic array of vortical cells, and meets seven stagnation points. Figure 8(*b*) shows the trajectory of the centre of mass of the fibre. As it approaches a stagnation point along a stable manifold, it bends, samples the local velocity field near this hyperbolic point, and exits along an unstable manifold. The

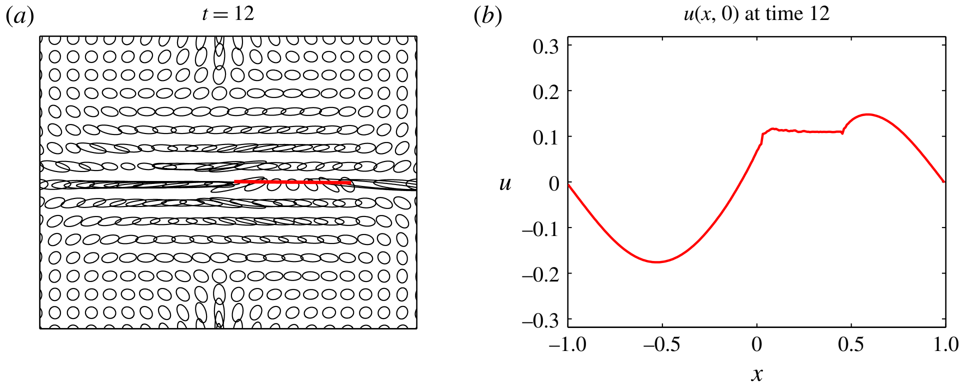

FIGURE 5. (Colour online) (*a*) Fibre and surrounding stress ellipse field at time $t = 12$. (*b*) Horizontal component of fluid velocity along x-axis at time $t = 12$.

direction along which the fibre exits is not predictable, as slight differences in the bending of the fibre can cause it to move in either direction. We quantify the buckling behaviour of the fibre as it moves through the domain in two ways. One measure, that is easiest to capture in physical experiments, is the distance between the fibre's endpoints, normalized by its equilibrium length. For a straight fibre, this scaled end-to-end length is one. In the context of our computational model, we can also measure fibre buckling by calculating its bending energy E_b in (2.8). Figure 6 shows these two measures of the fibre's bending over time. We can see that the fibre behaves similarly when it gets close to different stagnation points. As it moves towards the stagnation point, the scaled end-to-end length (figure 6*a*) abruptly decreases but moves back to one as the fibre straightens. Figure 6(*b*) shows similar behaviour with bending energy abruptly increasing as the fibre meets the stagnation points. Both measures of buckling show that there is a nearly constant transit time for the fibre to get from one stagnation point to another, but that the evolving shape deformation of the fibre is not periodic.

The time evolution of the bending energy in figure 6(*b*) reveals a curious, repeatable, 'blip' during the straightening phase. The bending energy spikes as the fibre reaches its maximum bent shape near the stagnation point, quickly decreases as the fibre straightens, but then increases a small amount until decreasing again. We now focus on the fibre's bending energy during its first trip in figure 7(*a*). Figure 7(*b*) shows the fibre configurations corresponding to the first peak of bending energy ($t = 6.1$), then at the smallest value of bending energy right before the blip ($t = 7.2$), and then at the second, smaller peak ($t = 7.9$). We see the fibre transition from its most bent configuration, straighten out, but then continue to bend in the recovery direction. One possibility for this overshoot in bending energy is the memory in the system due to both the inertia in the Navier–Stokes momentum conservation equation as well as the evolution of the stresses carried by the embedded polymers. Another possibility is that this blip is picking up the second peak in an exponentially damped sinusoidal solution of the classic elastic beam equation.

We note that in this immersed boundary framework, the fibre is not precisely inextensible, but imparts tensile forces to maintain its length. Although we choose a tensile coefficient large enough so that the fibre's arclength does not deviate more than 3 % of its equilibrium length, its realized arclength does vary. Figure 7(*a*) also

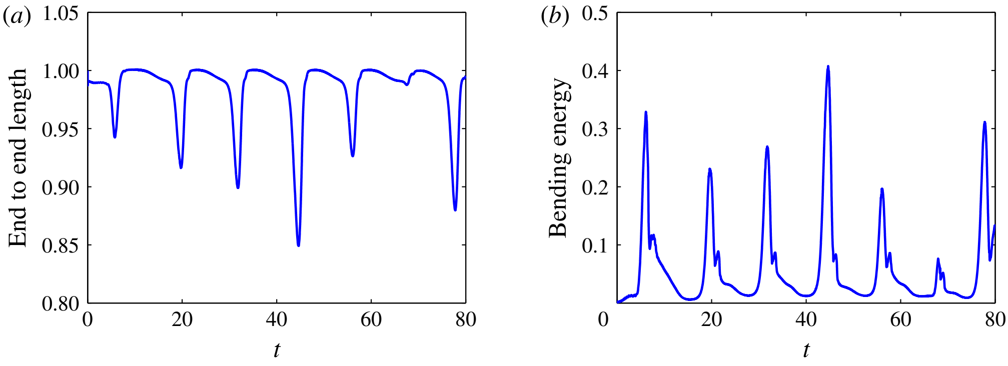

FIGURE 6. (Colour online) (*a*) The scaled end-to-end length of the fibre over time. (*b*) The bending energy of the fibre over time. Note that bending occurs periodically, but the details of the shape deformation are not periodic.

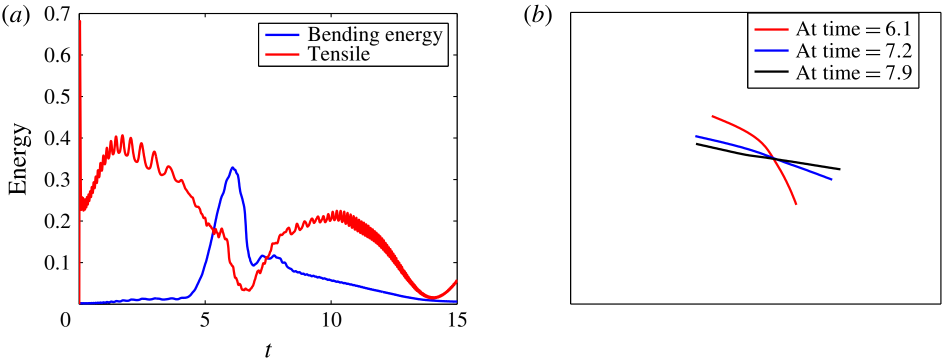

FIGURE 7. (Colour online) (*a*) Evolution of fibre bending energy and tensile energy during its first trip for time $0 \leqslant t \leqslant 15$. (*b*) Snapshots of fibre configurations during first trip that correspond to the first peak in bending energy, an intermediate time point, and then the second small peak in bending energy. Note that there is some overshoot of the straight equilibrium at the latest time point.

shows the evolution of the tensile energy E_t (2.8) during its first trip. When the fibre approaches the stagnation point it is almost straight, but the compression due to the flow generates significant tensile energy. We see that, during the time interval when the fibre is most bent, the tensile energy is at its lowest – the fibre struggles less to maintain its length during buckling.

4. Effect of Weissenberg number *Wi*

Here we examine the effects of varying the Weissenberg number of the coupled fibre–viscoelastic system while keeping the same Reynolds number ($Re = 2.5$) and elasto-viscous number of the fibre ($\eta = 370$) as in the previous example. In the absence of a macroscopic fibre, Thomases & Shelley (2007) showed that the strain rate at the stagnation point at steady state in the viscoelastic cellular flow decreased monotonically with *Wi* for the same background forcing. Since this strain rate governs the velocity time scales achieved in the cellular flow, we expect that fibre

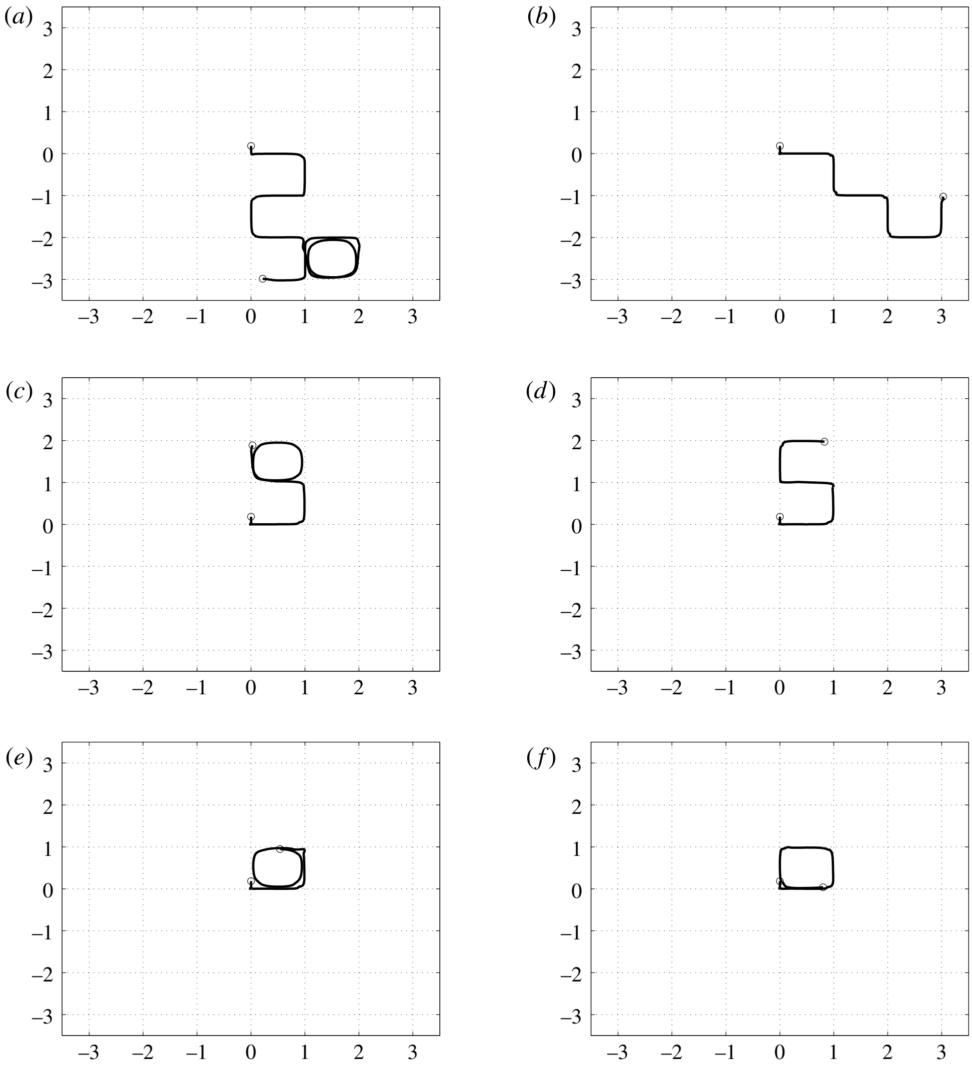

FIGURE 8. Trajectories of the centre of mass of the fibres for various *Wi*: (*a*) Newtonian, (*b*) $Wi = 1$, (*c*) $Wi = 2$, (*d*) $Wi = 3$, (*e*) $Wi = 4$ and (*f*) $Wi = 5$. Here $Re = 2.5$ and $\eta = 370$. Open circles indicate where they start and where they stop.

transport will slow down as viscoelasticity increases. We compare six simulations with Weissenberg number $Wi = 0$, 1, 2, 3, 4 and 5, noting that $Wi = 0$ corresponds to a Newtonian fluid. Initially each fibre was placed vertically, close to the centre stagnation point, but slightly off the incoming streamline as in figure 1(*a*). At each *Wi*, the qualitative motion of the fibres as they approached and moved away from the stagnation point was the same as that for the $Wi = 1$ example above. The fibre in the Newtonian fluid bends and moves away from the stagnation point first, followed monotonically by the fibres at increasing Weissenberg numbers. This monotonic arrival at stagnation points is also consistent with the observation by Thomases & Shelley (2007) that steady shear rates decrease with *Wi*. Figure 8 shows the trajectories of

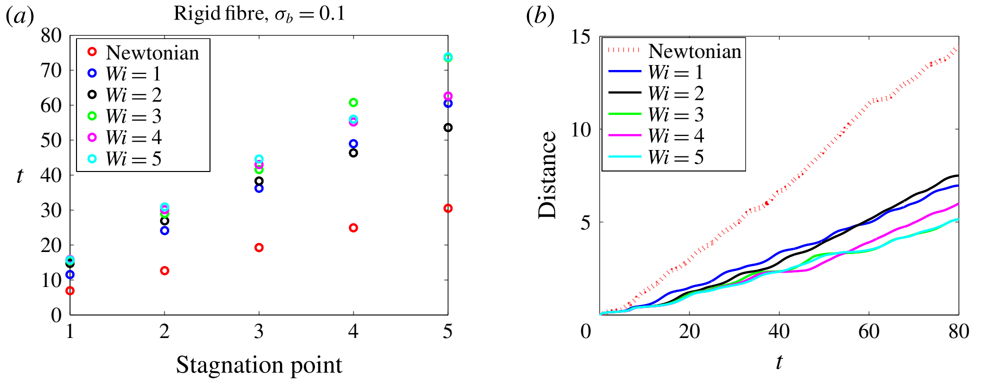

FIGURE 9. (Colour online) (*a*) Moment when the fibre arrives at successive stagnation points for different *Wi*. (*b*) Distance that the fibre's head travels up through time $t = 80$ for different *Wi*.

the centre of mass of each fibre at different *Wi* up to time $t = 80$, expanded to include many cells in the periodic domain. Open circles indicate both initial and terminal positions. While each fibre moves away from the first stagnation point it meets along the same outgoing streamline, their trajectories diverge after meeting the second stagnation point. As discussed by Young & Shelley (2007), the outgoing streamline along which the fibre leaves the area of the stagnation point is chosen with apparent randomness. Small fluctuations in the fluid environment and small changes in fibre bending easily alter the direction (Quennouz *et al.* 2015). Figure 8 indicates that, in the given time interval, the fibres in the Newtonian and smaller *Wi* flows are able to sample more of the spatial domain than the fibres in the higher *Wi* flows. In particular, the fibres at $Wi = 4$ and 5 are trapped in the cells where they were initially launched. We will revisit this feature of trapped fibres below.

The trajectories in figure 8 do not give information about the time scale of fibre transport. Figure 9(*a*) shows the moment when the fibre arrives at successive stagnation points. This is measured by monitoring the distance between the fibre's head and the stagnation points of the cellular domain. We see that for the first trip, the Newtonian one arrives at a stagnation point first, with the fibres at $Wi = 1$, 2, 3, 4 and 5 monotonically following. However, the evolving fibre geometries and deviation in chosen paths in the different *Wi* cases cause this monotonicity to be destroyed at later stagnation points. Figure 9(*b*) shows the total distance that the fibre's head travels as a function of time. Up until approximately $t = 40$, the distance travelled is monotonically decreasing in Weissenberg number. Deviations in the fibre paths and shape deformations again destroy this monotonicity at later times.

Because evolving fibre geometries and paths can vary greatly depending upon their initial placement and orientation (Quennouz *et al.* 2015), we restrict the comparison of the bending behaviours of fibres at different Weissenberg numbers to their first trip, as each is initialized identically. Figure 10(*a*) shows the bending energy of the fibres up to time $t = 15$. We see that the fibre in the Newtonian fluid bends earlier than the fibres at $Wi \neq 0$, and also meets its second stagnation point during this time interval at approximately $t = 11$. The Newtonian fibre has a larger bending energy than the fibres at $Wi \neq 0$ as it meets the stagnation point. While the time of buckling is monotonic in Weissenberg number, the bending energy is not. One feature of note,

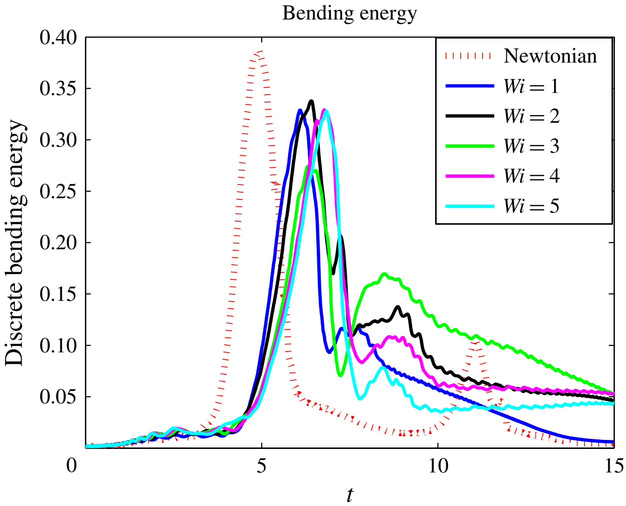

FIGURE 10. (Colour online) (*a*) Bending energy for the fibre at different *Wi* during the first trip. Here $Re = 2.5$ and $\eta = 370$.

however, is that the secondary peak of bending energy noted in the $Wi = 1$ case above is much more pronounced in the $Wi \neq 0$ cases, with only a slight blip appearing in the Newtonian case (figure 10*a*). This overshooting of curvature as the fibre straightens out is enhanced by the memory of polymer stresses distributed near the fibre.

5. Effect of elasto-viscous number η

Here we examine the effects of flexibility on fibre transport. We vary the non-dimensional bending coefficient σ_b of the fibre while keeping all the other parameters fixed for $Wi = 0$, 1 and 5. For bending coefficients $\sigma_b = 0.1$, 0.05, 0.025 and 0.0125, the elasto-viscous numbers are, respectively, $\eta = 370$, 740, 1480 and 2960. Early experiments by Forgacs & Mason (1959) classified the orbits of fibres in shear flow by tracking pulp, Dacron and elastomer fibres. Rigid rotations, springy rotations, snake turns and coil formations were described. We observe all these types of buckling behaviours when fibres with different elasto-viscous numbers are tracked at each $Wi = 0$, 1 and 5. Figure 11 shows snapshots of fibres of four stiffnesses as they traverse the cellular domain for $Wi = 0$ (*a*) and $Wi = 1$ (*b*). Each fibre was initially released at the same position. In each panel we superimpose successive positions of fibres of varying flexibility at equally spaced time intervals up through $t = 17$. The velocity field shown is the initial velocity field. As in the previous section, we are not able to discern a clear pattern of differences in fibre shape deformations with the same elasto-viscous numbers across *Wi* by comparing bending energy or scaled end-to-end lengths. However, fibre trajectories at all stiffnesses show significant qualitative differences with respect to the viscoelastic properties of the fluid.

In a four-roll-mill Newtonian flow with no immersed fibres, streamlines are closed in each cellular region. A point particle will simply follow a vortical streamline and never escape the cell in which it was launched. However, a finite-length fibre generates forces to alter the surrounding velocity field and can cross streamlines, allowing for the possibility of escape. Young & Shelley (2007) studied the transport of fibres in Newtonian cellular flows and identified a region within the cell such that,

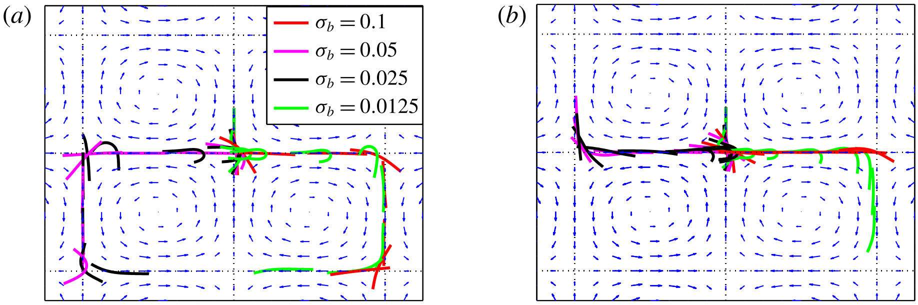

FIGURE 11. (Colour online) Fibre configurations in (*a*) Newtonian fluid and (*b*) $Wi = 1$ at different times. For bending coefficients $\sigma_b = 0.1$, 0.05, 0.025 and 0.0125, the elasto-viscous numbers are, respectively, $\eta = 370$, 740, 1480 and 2960. Note that each panel represents the results of four simulations, with each of the fibre positions at the times $t = 1$, 3, 5, 7, 9, 11, 13, 15 and 17.

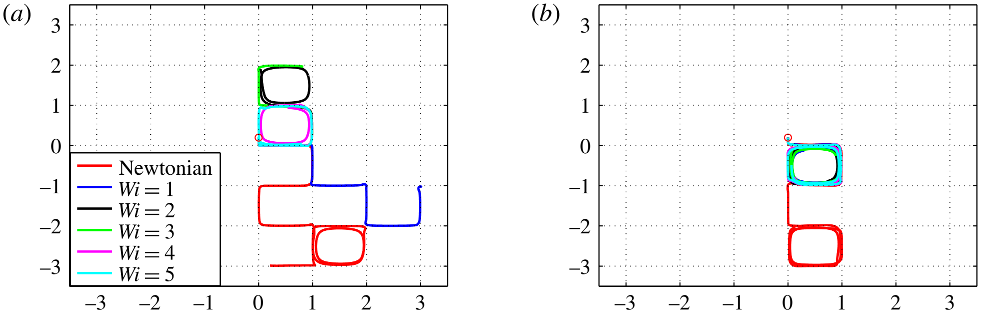

FIGURE 12. (Colour online) Trajectories of centre of mass of fibres for different Wi through time $t = 80$. (*a*) Stiffest fibre $\sigma_b = 0.1$ ($\eta = 370$). (*b*) Most flexible fibre $\sigma_b = 0.0125$ ($\eta = 2960$). In all cases the trajectories begin at the spatial position $(3 \times 10^{-3}, 3 \times 10^{-6})$ (open circle).

when the fibre is launched in that region, it remains trapped. The experiments of Wandersman *et al.* (2010) varied the distance between the fibre placement and the vertical centreline and measured the number of trajectories required for the fibre to escape. They found that flexible fibres escaped the original cell more frequently than rigid fibres. Quennouz *et al.* (2015) expanded these experiments and concluded that escape is determined not only by the elasto-viscous number, but also by the fibre's entry position and orientation.

For fibres launched close to the incoming streamline, as in figure 1(*a*), figure 12(*a*) shows the trajectories of the most rigid fibre ($\eta = 370$) in simulations of different Wi and figure 12(*b*) shows the corresponding trajectories of the most flexible fibre ($\eta = 2960$). There are some important features to note. The most rigid and most flexible fibres at $Wi = 4$ and 5 remain trapped in a cellular region. All the flexible fibres at each Wi are able to escape the original cell in which they were launched. This is consistent with the observations in Wandersman *et al.* (2010). However, for $Wi \neq 0$, all of these flexible fibres remain trapped in the second cell they encounter. The most

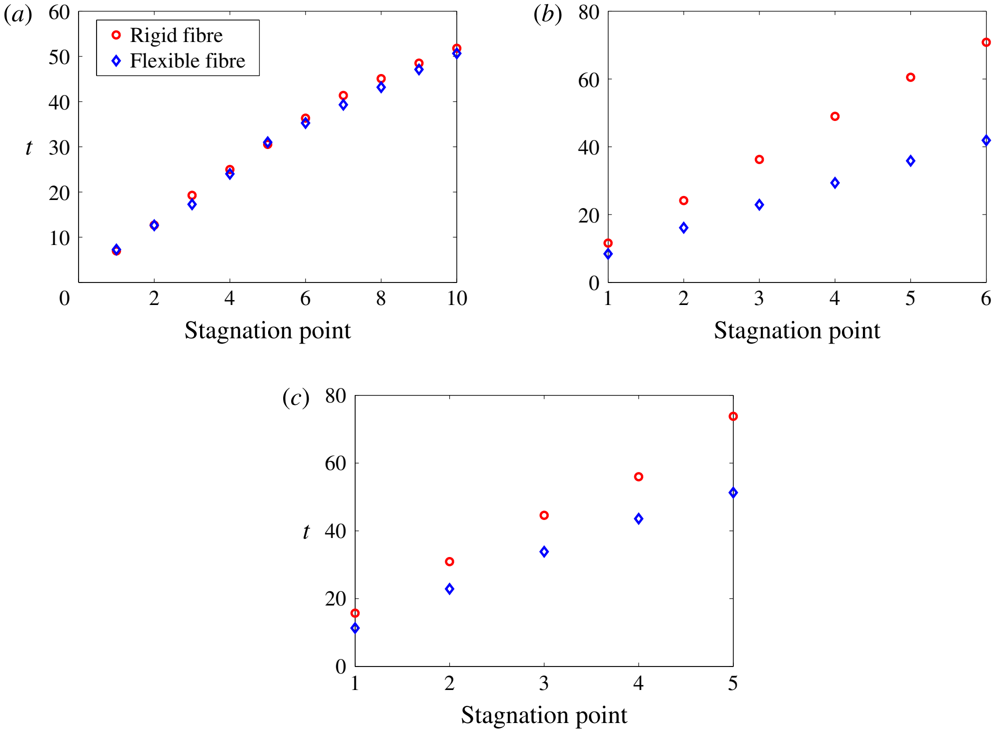

FIGURE 13. (Colour online) Times at which the most rigid fibre and the most flexible fibre arrive at successive stagnation points at different Weissenberg number: (*a*) $Wi=0$ (Newtonian), (*b*) $Wi=1$ and (*c*) $Wi=5$.

rigid fibres at $Wi=0$, 1 do not remain trapped in any cell up through the simulation time $t=80$. In contrast, the most rigid and most flexible fibres at $Wi=4$ and 5 remain trapped in a cellular region as they leave the first stagnation point.

Figure 13 tracks the moment when the most rigid and most flexible fibres arrive at successive stagnation points (which could be repeated) in Newtonian, $Wi=1$ and $Wi=5$ flows. The rigid fibre always lags behind the flexible fibre in arrival times, and this is more pronounced at $Wi\neq 0$. Note that, for the case $Wi=1$, the rigid fibre is traversing multiple cells, while the flexible fibre remains trapped.

We performed systematic studies that varied the initial placement of both the rigid fibre $\sigma_b=0.1$ and the flexible fibre $\sigma_b=0.0125$ within the vortical cell, at Weissenberg numbers $Wi=0$, 1, 2, 3, 4 and 5. The fibres were always launched vertically in their straight equilibrium shape, along $x=b$, where b varied from 0.01 to 0.09, and the lower point of the fibre was at $y=0.5$. For all initial placements of the most rigid fibres, the fibres in the Newtonian fluid eventually escaped the original cell. When placed well within the vortical cell, even the fibre in the $Wi=1$ case remains trapped when $b\geqslant 0.07$. For all values of b, the rigid fibres in the $Wi=4$ and 5 cases never escape. For the most flexible fibres, when initialized well within the cell, no fibre escaped – even in the Newtonian case. However, when placed further at the cell periphery, the flexible fibre does escape in the Newtonian case, but those in the non-zero Wi cases do not.

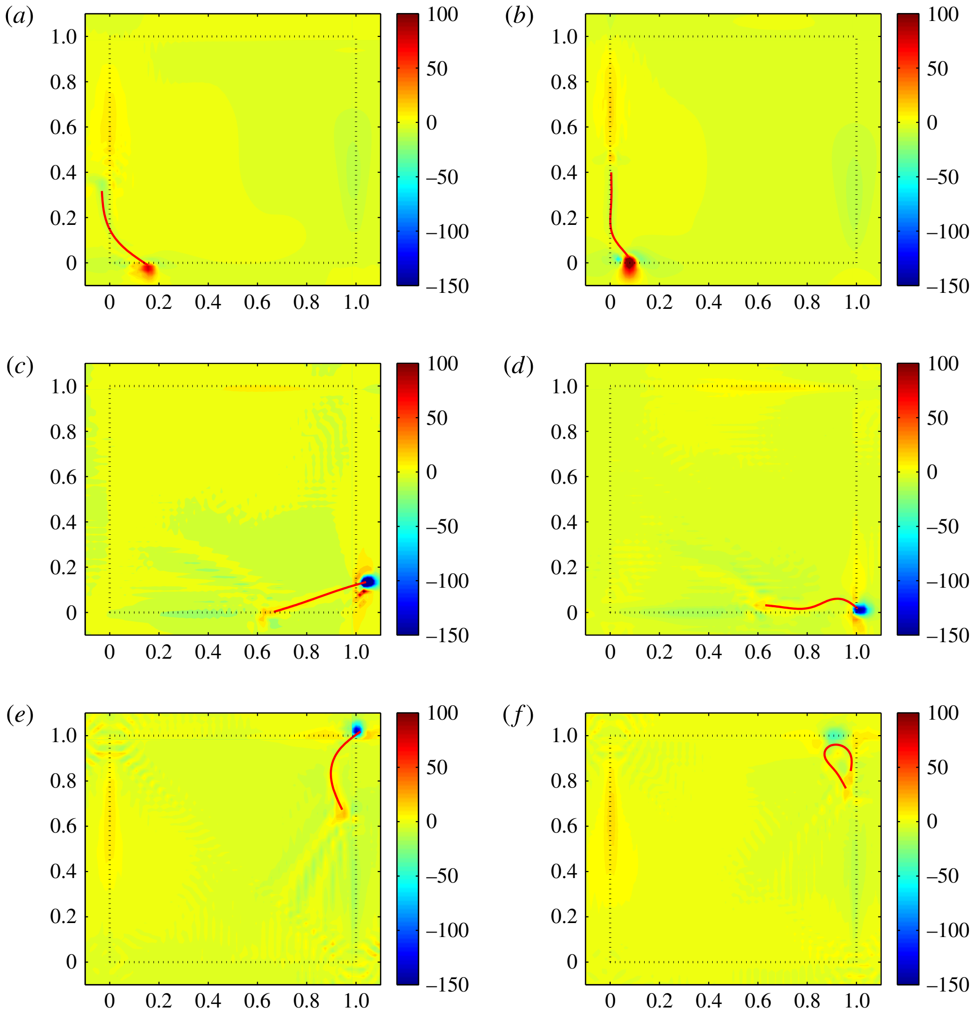

FIGURE 14. (Colour online) Contours of polymer force densities when the most rigid fibre (*a*,*c*,*e*, $\eta = 370$) and most flexible fibre (*b*,*d*,*f*, $\eta = 2960$) move in the cellular flow at $Re = 2.5$ and $Wi = 3$: (*a*) y-component, $\eta = 370$, $t = 4$; (*b*) y-component, $\eta = 2960$, $t = 2.5$; (*c*) x-component, $\eta = 370$, $t = 15$; (*d*) x-component, $\eta = 2960$, $t = 14$; (*e*) y-component, $\eta = 370$, $t = 25$ and (*f*) y-component, $\eta = 2960$, $t = 25$.

To understand why the presence of the polymers in viscoelastic fluids hinders the fibre's ability to escape, we examine the force densities $\beta \nabla \cdot \boldsymbol{S}$ that are generated by the polymers. Figure 14 shows the contour plot for these polymer force densities in the x- and y-directions for the most rigid fibre (left column) and the most flexible fibre (right column) at instances where the fibre is near the edge of the cellular region ($Wi = 3$). In figure 14(*a*,*b*), when the fibres are near the bottom edge, large positive y-components of polymer force density (outward y-direction) are generated near the fibre's head and push the fibre back into the cell. When the fibres are near the right edge (figure 14*c*,*d*), large negative x-components of polymer force density (inward x-direction) are generated, again impeding escape. At time $t = 25$, figure 14(*e*) shows that large force densities in the inward y-direction push back the most rigid fibre, which does get trapped in the cell as time progresses. Figure 14(f) shows that at the same time $t=25$ the most flexible fibre is already deep into the cellular region, and large force densities are not required to keep it confined to the cell.

6. Conclusions

We have modelled the motion of a macroscopic fibre in a viscoelastic fluid in a doubly periodic cellular flow and compared its dynamics to that in a Newtonian fluid. Because of overall flow time scales, the fibre in a Newtonian fluid travels faster and buckles earlier than in the viscoelastic fluids. In viscoelastic flows, we find that polymer stresses are highly concentrated near the fibre's ends when the fibre is straight. However, they are distributed along the fibre when the fibre buckles. The occupation of the fibre at the centre stagnation point limits the stretch of the polymers there. As in the Newtonian case, fibre trajectories through the doubly periodic domain depend on their elasto-viscous number and their initial positioning and orientation. These simulations show that viscoelasticity greatly hinders a fibre's ability to escape cellular regions. We examine the polymer stress field, and note that for larger Weissenberg numbers the embedded polymers generate large forces to push the fibre back into the cell when the fibre is near its edge.

The dynamics of the coupled fibre–viscoelastic fluid system presented here are two-dimensional. Hence, the fibre may be regarded as an elastic sheet of finite extent. Nevertheless, the fibre buckling and transport behaviours observed in these simulations are in general agreement with the slender-body simulations of Young & Shelley (2007) and Tornberg & Shelley (2007), where the fibre centrelines were confined to a plane but the viscous fluid dynamics was three-dimensional. However, the fully three-dimensional simulations of Nguyen & Fauci (2014) that represent the fibre surface along with its centreline demonstrate that out-of-plane perturbations of the fibre centreline in linear shear flow give rise to complex coiled shapes. Future implementation of a fully three-dimensional macroscopic fibre immersed in a polymeric cellular flow will determine if there are other qualitative features of the coupled system that have not been captured by the two-dimensional simplification.

The computational studies presented here have elucidated some features of the effects of viscoelasticity on fibre buckling and transport by varying both the Weissenberg number and the elasto-viscous number of the fibre. Future investigations will investigate how the dynamics of this fibre–viscoelastic system change with the presence of additional macroscopic fibres. We look forward to the extension of laboratory studies as in Wandersman *et al.* (2010) and Quennouz *et al.* (2015) to include viscoelastic fluids that will shed light on these intriguing complex systems.

REFERENCES

BALCI, N., THOMASES, B., RENARDY, M. & DOERING, C. R. 2011 Symmetric factorization of the conformation tensor in viscoelastic fluid models. *J. Non-Newtonian Fluid Mech.* **166**, 546–553.

BECKER, L. E. & SHELLEY, M. 2001 Instability of elastic filaments in shear flow yields first-normal stress differences. *Phys. Rev. Lett.* **87**, 198301.

CHRISPELL, J. C., FAUCI, L. & SHELLEY, M. 2013 An actuated elastic sheet interacting with passive and active structures in a viscoelastic fluid. *Phys. Fluids* **25**, 013103.

FAUCI, L. & DILLON, R. 2006 Biofluidmechanics of reproduction. *Annu. Rev. Fluid. Mech.* **38**, 371–394.

FORGACS, O. L. & MASON, S. G. 1959 Particle motions in sheared suspensions: X Orbits of flexible threadlike particles. *J. Colloid Sci.* **14**, 473–491.

HARASIM, M., WUNDERLICH, B., PELEG, O., KROGER, M. & BAUSCH, A. 2013 Direct observation of the dynamics of semiflexible polymers in shear flow. *Phys. Rev. Lett.* **110**, 108302.

KANTSLER, V. & GOLDSTEIN, R. 2012 Fluctuations, dynamics, and the stretch–coil transition of a single actin filament in extensional flow. *Phys. Rev. Lett.* **108**, 038103.

KARP-BOSS, L. & JUMARS, P. A. 1998 Motion of diatom chains in steady shear flow. *Limnol. Oceanogr.* **43** (8), 1767–1773.

LAI, M.-C. & PESKIN, C. S. 2000 An immersed boundary method with formal second order accuracy and reduced numerical viscosity. *J. Comput. Phys.* **160**, 705–719.

LARSON, R. G. 1998 *The Structure and Rheology of Complex Fluids*. Oxford University Press.

MANIKANTAN, H. & SAINTILLAN, D. 2013 Subdiffusive transport of fluctuating elastic filaments in cellular flow. *Phys. Fluids* **25**, 073603.

NGUYEN, H. & FAUCI, L. 2014 Hydrodynamics of diatom chains and semiflexible fibres. *J. R. Soc. Interface* **11**, 20140314.

PESKIN, C. S. 2002 The immersed boundary method. *Acta Numerica* **11**, 479–517.

PHAN-THIEN, N. 2002 *Understanding Viscoelasticity*. Springer.

QUENNOUZ, N., SHELLEY, M., DU ROURE, O. & LINDNER, A. 2015 Transport and buckling dynamics of an elastic fibre in a viscous cellular flow. *J. Fluid Mech.* **769**, 387–402.

SKJETNE, P., ROSS, R. F. & KLINGENBERG, D. J. 1997 Simulation of single fiber dynamics. *J. Chem. Phys.* **107**, 2108.

STOCKIE, J. & GREEN, S. 1998 Simulating the motion of flexible pulp fibres using the immersed boundary method. *J. Comput. Phys.* **147**, 147–165.

TERAN, J., FAUCI, L. & SHELLEY, M. 2010 Viscoelastic fluid response can increase the speed and efficiency of a free swimmer. *Phys. Rev. Lett.* **104**, 038101.

THOMASES, B. & GUY, R. D. 2014 Mechanisms of elastic enhancement and hindrance for finite-length undulatory swimmers in viscoelastic fluids. *Phys. Rev. Lett.* **113**, 098102.

THOMASES, B. & SHELLEY, M. 2007 Emergence of singular structures in Oldroyd-B fluids. *Phys. Fluids* **19**, 103103.

TORNBERG, A. K. & SHELLEY, M 2007 Simulating the dynamics and interactions of elastic filaments in Stokes flow. *J. Comput. Phys.* **196**, 8–40.

WANDERSMAN, E., QUENNOUZ, N., FERMIGIER, M., LINDNER, A. & DU ROURE, O. 2010 Buckled in translation. *Soft Matt.* **6**, 5715–5719.

YOUNG, Y. N. & SHELLEY, M. 2007 Transition and transport of fibers in cellular flows. *Phys. Rev. Lett.* **99**, 058303.